Modelling Static and Dynamic FRP-Concrete Bond Behaviour Using a Local Concrete Damage Model

Modelling static and dynamic FRP-concrete bond behaviour using a local concrete damage model

Xiaoqin Li [1], Jian-Fei Chen [2,*], Yong Lu [3] and Zhenjun Yang [4]

[1] Faculty of Civil Engineering

Kunming University of Science and Technology, Kunming, China.

[2] School of Planning, Architecture and Civil Engineering, Queen's University Belfast, Belfast, UK.

[3] Institute for Infrastructure and Environment, School of Engineering, University of Edinburgh, Edinburgh, UK.

[4] College of Civil Engineering and Architecture, Zhejiang University, Hangzhou, China.

Abstract:

This paper presents a study on the bond behaviour of FRP-concrete bonded joints under static and dynamic loadings, by developing a meso-scale finite element model using the K&C concrete damage model in LS-DYNA. A significant number of single shear experiments under static pull-off loading were modelled with an extensive parametric study covering key factors in the K&C model, including the crack band width, the compressive fracture energy and the shear dilatation factor. It is demonstrated that the developed model can satisfactorily simulate the static debonding behaviour, in terms of mesh objectivity, the load-carrying capacity and the local bond-slip behaviour, provided that proper consideration is given to the selection of crack band width and shear dilatation factor. A preliminary study of the effect of the dynamic loading rate on the debonding behaviour was also conducted by considering a dynamic increase factor for the concrete strength as a function of strain rate. It is shown that a higher loading rate leads to a higher load-carrying capacity, a longer effective bond length, and a larger damaged area of concrete in the single shear loading scenario.

Key words: FRP-concrete bond; K&C concrete damage model; localization; dilatation; dynamic increasing factor (DIF); loading rates; bond test; dynamic bond-slip model.

*Corresponding author. Email address: J.Chen@qub.ac.uk; Fax: +44 28 9097 4278; Tel: +44 (0)28 9097 4184.

1 INTRODUCTION

Fibre reinforced polymer (FRP) composites have been used for strengthening concrete structures since the early 1990s and the technique is now very popular worldwide. More recently, FRP has been used to retrofit concrete structures against dynamic loadings such as impact (Bhatti *et al.* 2011; Boyd *et al.* 2008), blast (Heffernan *et al.* 2011; Wu *et al.* 2009; Buchan and Chen 2007; Crawford *et al.* 1997) and earthquake (Niroomandi *et al.* 2010; Pantelides and Gergely 2007; Teng *et al.* 2007). These studies have confirmed that FRP retrofitting is effective in increasing the structural resistance against these dynamic loadings as well as preventing fragmentation-induced damage to people and properties. It has also been observed that, as for static loading cases, debonding on the FRP-concrete interface is one of the predominant failure modes under dynamic loadings. However, most of early studies were either experimental (Tarapada and Debabrata 2006) or macro-scale numerical simulations focused on the global structural behaviour (Crawford *et al.* 2001), with limited analytical investigation (De Lorenzis and La Tegola 2005). Little attention has been paid to the critical FRP-concrete interfacial bond behaviour under dynamic loadings.

The dynamic bond behaviour could be very different from that under static or quasi-static loadings because of the effects of higher strain rate, as well as damage to concrete due to propagation of intense stress wave ahead of global deformation-induced debonding or FRP fracture. Accurate quantification of these effects by experiments is very demanding both economically and technically, especially for high loading rate scenarios such as impact and blast. On the other hand, the advancement of finite element (FE) techniques tends to provide a seemingly viable tool for high fidelity numerical investigation into such complex phenomenon.

Many static FE studies have been conducted for concrete structures strengthened by FRP composites (Chen *et al.* 2011, 2012; Kim and Vecchio 2008; Lu *et al.* 2004; Yang *et al.* 2003; Teng *et al.* 2002; Chen and Teng 2001). Because most debonding failures occur in the concrete adjacent to the FRP, rather than in the adhesive layer, or at the FRP-adhesive or adhesive-concrete interfaces, the modelling of concrete damage and fracture is of crucial importance for any reasonable prediction of the bond behaviour.

There are mainly two approaches for modelling concrete cracking in FE analysis: the smeared crack model based on continuum mechanics (Bazant and Oh 1983) and the discrete crack model explicitly modelling discontinuity (Yang *et al.* 2003). Although the latter is capable of modelling individual macro-cracks, the need of re-meshing (Yang *et al.* 2003) or embedding cohesive elements (Su *et al.* 2010; Yang *et al.* 2009) makes it cumbersome to model a large number of meso-scale distributed cracks during debonding in FRP-strengthened concrete structures. The smeared crack model is more suitable for such cases because it does not require re-meshing and can make use of concrete stress-strain curves that are readily available for static and dynamic loadings. This model has indeed been adopted in most of existing studies (Chen *et al.* 2011, 2012; Chen and Tao 2010; Lu *et al.* 2004, 2005) to investigate the meso-scale debonding behaviour of FRP-concrete joints. However, all these studies considered static or quasi-static loadings only.

There are two classes of smeared crack models, local (Lubliner 1989) and non-local (Bazant and Ozbolt 1990; Bazant and Pijaudier-Cabot 1988). Concrete damage is calculated in each element independently in the former, whereas in the latter damage calculation in an element takes into account the stiffness degradation in its surrounding elements, depending on a specified crack band width and the element size. The crack band width, often approximated as three times the maximum aggregate size under static loading (Bazant and Oh 1983), may be regarded as a material property. However, no consensus on its value has been reached for dynamic loadings due to the lack of reliable experimental data. In FRP-bonded concrete structures under static loading, debonding usually occurs at 2-5*mm* depth of the concrete adjacent to the FRP (Lu *et al.* 2004). This depth is smaller than the aggregate size of 10-40*mm* in normal strength concrete, and much smaller than the assumed crack band width, making the non-local models unsuitable for modelling the FRP-concrete debonding behaviour.

This study develops a finite element model based on the K&C local damage concrete model in LSDYNA (LSTC 2007; Malvar *et al.* 2000; Malvar *et al.* 1997; Malvar and Simons 1996) for an appropriate prediction of debonding behaviour of the FRP-concrete bonded joint. The model was first validated against various laboratory experiments under static pull-off tests. It was then applied to numerically investigate the dynamic pull-off behaviour under high strain rate loadings.

2 THE K&C CONCRETE DAMAGE MODEL

The finite element package LSDYNA Explicit (LSTC 2007) was chosen in this study considering its capability in modelling high energy events such as blast and impact loadings. The concrete material was modelled by an enhanced version (material #72_Rel3 in LSDYNA v971) of the K&C concrete damage model (Malvar *et al.* 1997). The model is regarded as one of the most comprehensive damage plasticity models for concrete-like materials in transient analysis codes and has been widely used (Tu and Lu 2009).

The K&C model uses three independent strength surfaces, namely, an initial yield surface, a maximum failure surface and a residual surface with consideration of three stress invariants, I_1, J_2 and J_3. The compressive meridians of the three surfaces are defined in terms of the effective deviatoric stresses ($\Delta\sigma = \sqrt{3J_2}$) independently as (Malvar *et al.* 1997):

initial yield failure surface: $$\Delta\sigma_y = a_{0y} + \frac{p}{a_{1y} + a_{2y}} \quad (1)$$

maximum failure surface: $$\Delta\sigma_m = a_0 + \frac{p}{a_1 + a_2} \quad (2)$$

residual failure surface: $$\Delta\sigma_r = \frac{p}{a_{1f} + a_{2f}} \quad (3)$$

where $\Delta\sigma_y, \Delta\sigma_m$ and $\Delta\sigma_r$ are functions of the mean pressure $p = I_1/3$, in which I_1 is the first invariant of stress tensor, and the coefficients a_{0y}, a_{1y}, a_{2y}, a_0, a_1, a_2, a_{0f}, a_{1f} and a_{2f} are considered as material constants and can be determined from experiments

(Malvar *et al.* 1997). During an analysis, the current failure surface $\Delta\sigma$ is interpolated between the maximum failure surface, $\Delta\sigma_m$ and either the yield $\Delta\sigma_y$ or the residual failure surface $\Delta\sigma_r$ as:

$$\Delta\sigma = \eta\Delta\sigma_m + (1-\eta)\Delta\sigma_y \text{ when } \lambda \le \lambda_m \tag{4}$$

$$\Delta\sigma = \eta\Delta\sigma_m + (1-\eta)\Delta\sigma_r \text{ when } \lambda > \lambda_m \tag{5}$$

where the damage accumulation parameter η is a user-defined function of a modified effective plastic strain measure λ. The concrete model requires user input of a series of (λ,η) pairs to describe the function $\eta(\lambda)$ which shall first increase from an initial value, i.e. 0, before any plasticity has occurred, to 1.0 at the maximum failure surface, and then decrease (softening) to 0 at the residual failure surface. The initial yield surface is given by:

$$\Delta\sigma_y = \eta_y\Delta\sigma_m + (1-\eta_y)\Delta\sigma_r \tag{6}$$

where $\eta_y = \eta(0)$ is the initial value of η (Malvar *et al.* 1997; Malvar and Simons 1996). The modified effective plastic strain λ is calculated as:

$$\lambda = \int_0^{\bar{\varepsilon}^p} \frac{d\bar{\varepsilon}^p}{r_f(1+p/r_f f_t)^{b_1}} \qquad for \qquad p \ge 0 \tag{7}$$

$$\lambda = \int_0^{\bar{\varepsilon}^p} \frac{d\bar{\varepsilon}^p}{r_f(1+p/r_f f_t)^{b_2}} \qquad for \qquad p < 0 \tag{8}$$

where $d\bar{\varepsilon}^p = \sqrt{(2/3)d\varepsilon_{ij}^p d\varepsilon_{ij}^p}$ is the effective plastic strain increment, ε_{ij}^p is the three-dimensional plastic strain state of the material, f_t the quasi-static concrete tensile strength, r_f the strain rate enhancement factor, b_1 and b_2 the parameters controlling the softening part of the stress strain curve. A scaled damage factor (*SDF*) is defined to measure the damage:

$$SDF = \frac{2\lambda}{\lambda + \lambda_m} \tag{9}$$

where λ_m is the value of λ at the maximum failure surface (η=1). *SDF* is a positive non-decreasing variable: 0< *SDF* <1 means no damage, *SDF* >1 represents damage with material softening, and *SDF* =2 full damage.

In LSDYNA, the user may only input the unconfined compressive strength f_c', in which case all other material parameters for the K&C concrete damage model can be automatically generated. Schwer and Malvar (2005) highlighted that these automaticly generated parameters were calibrated using the well characterized 45.6*MPa* unconfined compression strength concrete for which uni-axial, bi-axial, and tri-axial test data in tension and compression are available, and this concrete strength is commonly used as the 'standard concrete' in many numerical simulations. Whilst this makes the concrete model simple to use and it generally produces a robust representation of many response characteristics of this complex material, including damage and failure, care needs to be exercised where the concrete differs significantly

from the 'standard concrete' in which case additional model parameter calibration is required (Markovich *et al.* 2011; Schwer and Malvar 2005).

3 FE MODELLING OF STATIC SINGLE SHEAR TEST

3.1 *The FE model*

The FRP-to-concrete bond behaviour is commonly tested using the single pull-push shear (or pull-off) test in which a plate is bonded to a concrete prism and is subject to tension (Chen *et al.* 2001) (Figure 1). The test specimen S-CFS-400-25 reported in Wu *et al.* (2001) was used as the reference case in this study. The specimen consisted of a 275×100×100*mm* (length × width × depth) concrete prism bonded with a 0.22*mm* thick and 40*mm* wide FRP sheet with a bond length of 250*mm*. The concrete had a cylinder compressive strength of 57.6*MPa*. The FRP had a modulus of elasticity of 230*GPa*.

There are generally two approaches to modelling debonding in FRP-strengthened RC structures: one is to employ a layer of interface elements between the FRP and the concrete, in which debonding is simulated as the failure of the interface elements. This approach requires the use of a bond-slip model for the interface elements which is therefore not really predictive. Another approach is direct modelling of cracking and failure of concrete adjacent to the FRP. This approach is valid when debonding failure occurs in the concrete (as in most test observations), and has the capability of predicting the bond-slip relationship (Lu *et al.* 2004). The aim of this study was to establish an accurate predictive FE model for static loading and use it to explore the effect of dynamic bond-slip behaviour. Therefore, the second approach is adopted.

The present FE model adopted the same geometry and boundary conditions as those in Lu *et al.*'s (2004) (Figure 1). Meshes with an element size of 2.5*mm*, 1*mm* and 0.5*mm*, respectively, were chosen for mesh convergence analysis in this study. The test was modelled as a two-dimensional (2D) plane stress problem but the predicted results including loads, stresses, strains and slips were corrected according to Chen and Teng's (2001) width effect factor to consider the three-dimensional (3D) effects.

The K&C concrete model employed in this study only works in a 3D setting. In the present model both the FRP plate and the concrete were modelled using the eight node hexahedron 3D solid elements. The width direction of the test specimen (z direction in Figure 1) was represented by a single element of thickness equal to the element side length. The model thus consists of a single layer of elements. All nodes on one face (at z =0) of this layer of elements were restrained for displacement in the z direction to simulate the plane stress condition.

The FRP was modelled as an isotropic linear elastic material with a thickness t_f =1*mm* and Young's modulus E_f = 50.6*GPa* so that its axial rigidity $E_f t_f$ remains the same as in the test. Because debonding of FRP in the single shear test usually occurs at a small distance beneath the adhesive-concrete interface in the concrete, the FRP was assumed to be perfectly bonded to the concrete prism in the current study. The specimen was loaded with a time dependent displacement at the loaded end in the FE model.

It should be noted that the K&C concrete damage model is a smeared crack band model with a default localisation width l_w =25.4*mm*, which is presumably applicable when the characteristic length of the elements is larger than 25.4*mm*. However, if the element size is smaller than l_w, the model will internally use l_w in defining the softening rate, consequently mesh objectivity becomes problematic. In such cases, l_w should reasonably be set equal to the element characteristic length h_c, so that the Mode I fracture energy G_f^I as a material constant may be preserved in each element. That is to say, the following equation is maintained in the simulation when l_w is made equal to h_c:

$$\int \sigma d\varepsilon = \frac{G_f^I}{h_c} \tag{10}$$

The parameter b_2 in the K&C concrete damage model (Eqn 7) governs the basic softening branch of the concrete under uni-axial tension. Its default value is 1.35 based on laboratory material characterization of 45.6*MPa* concrete mentioned before. However, this default value may not produce the correct fracture energy G_f^I when the concrete strength is different, therefore the b_2 value may need to be adjusted accordingly. Generally, a reduction in b_2 increases G_f^I. For the concrete used in the reference experiment, G_f^I was calculated to be 102*N/m* according to CEB-FIP (1993). To produce this value, b_2 was set to 0.45. The parameter b_1 was set as 1.6 so that the compressive fracture energy is approximately 100 times the tensile fracture energy (Li 2012). All the concrete parameters for the reference case are listed in Table 1.

3.2 *FE calibration factor according to Chen and Teng's model*

As mentioned earlier, the numerical model for the pull-off test was simplified as a 2D plane stress problem, where the widths of the FRP and concrete are the same. However in the original experiment, the actual width of FRP plate, b_{ft}, and the width of the concrete prism, b_{ct}, of the test specimen were 40*mm* and 100*mm*, respectively. In the current FE model, both widths were treated equal to the thickness of the model. This implies that the different width effect as in the actual experiment was not represented in the numerical model. To compensate for this effect, the FE results are corrected according to Chen and Teng's (2001) width effect by multiplying β_t for actual b_{ft} and b_{ct} values and dividing by β_t for b_{ft} = b_{ct} =1, with:

$$\beta_t = \sqrt{\frac{2 - b_{ft}/b_{ct}}{1 + b_{ft}/b_{ct}}} \tag{11}$$

3.3 *Static modeling and results*

The simulation was conducted using the explicit time integration method for the static test, consistent with the dynamic modelling to be presented later in the paper. When an explicit solver is used to model static and quasi-static problems, the loading time shall be long enough to avoid the dynamic effect, but not too long for computational

efficiency. The computational demand is mainly controlled by the time step and the total loading time. The largest time step Δt_{cr} without causing numerical instability is usually the time for the P-wave to travel through the smallest element in the model. As far as the global response is concerned, the dynamic effect becomes negligible when the total loading time is greater or equal to $10T$, where T is the fundamental period of the structure (Chen *et al.* 2009). A smooth velocity loading is advantageous because it enables a zero initial acceleration, in addition to zero initial displacement and velocity. In simulating the static test specimens in this study, a smooth velocity loading history was generated so that it produced a maximum displacement of 1.6*mm* at the loaded end of the FRP by the end of the loading phase, similar to the reference experiment. More details can be found in (Li *et al.* 2010).

Figure 2 shows the predicted load-slip response for three different trial meshes. It can be seen that the loading capacity increases with the reduction of the mesh size in general but the difference was already very small between those from the 1*mm* and 0.5*mm* meshes. The peak load 14.5*kN* predicted from the 0.5*mm* mesh is very close to the test result 14.1*kN* and a previous FE prediction of 13.8*kN* by Lu *et al.*'s (2004). The prediction by Chen and Teng's (2001) model is 11.4*kN*. The model is therefore regarded to be capable of simulating the static FRP-to-concrete bond behaviour with good accuracy. All meshes successfully reproduced the debonding failure as observed in the test. Figure 3 shows the damage contours at different loading stages for the 0.5*mm* mesh.

The FE results from the 0.5*mm* mesh are further analysed here in terms of the FRP strain distribution and the bond-slip relationship. Figure 4 shows that the FRP strain distributions at different loading levels are in close agreement with the test data of Wu *et al.* (2001) and the FE predictions of Lu *et al.* (2004). Note that the load has been normalised in Figure 4 by their respective ultimate load P_u from the three studies.

Figure 5 shows the local bond-slip relationship obtained at 19.5*mm* from the loaded end using the following equation:

$$\tau = \frac{\Delta \sigma_f}{\Delta x} t_f \tag{12}$$

in which τ is the local bond (shear) stress, $\Delta \sigma_f$ the difference of axial stress between two adjacent FRP elements, Δx the length of the FRP element, and t_f the thickness of the FRP plate. Shown for comparison are also the bond-slip curves obtained from the test and from a previous FE analysis (Lu *et al.* 2004) and using a "simplified model" (Lu *et al.* 2005). The area under the local bond-slip curve predicted in this study is slightly larger than that of the previous FE prediction, but close to that under the bi-linear curve deduced from the test data.

It should be noted that the bond-slip curve obtained from an FE analysis is different at one location from another and it also depends on the relative position to the micro-cracks in the concrete. Therefore it is difficult to judge from such results predicted from different FE models. The bi-linear bond-slip curve in Figure 5 was deduced from the experiment based on the maximum load and it represents an average of the local bond-slip relation over the bond length. The maximum bond stress is evaluated according to the following equation:

$$\tau_{\max} = \frac{P_u^2}{E_f t_f b_{ft}^2 \delta_f} \tag{14}$$

where $\tau_{\max}$ is the peak value of the bond stress; P_u is the ultimate load applied on the FRP; E_f is the elastic modulus of the FRP; t_f is the thickness of the FRP; b_{ft} is the width of the FRP; and δ_f is the slip at which the bond stress reduces to zero.

4 SHEAR DILATION

Dilation is a measure of volume increase when a material is under shear. In the Mohr-Coulomb material model, a dilation angle α is specified in a range from zero to the internal friction angle φ. For associated flow rules $\alpha = \varphi$. The two are not equal for non-associated flow rules. According to Chandra *et al.* (2010), soft rocks usually have lower dilation angles while hard brittle rocks have higher values. A good starting estimate is $\alpha = \varphi/3$ for soft rocks and $\alpha = 2\varphi/3$ for hard rocks, and zero for very weak rocks. It appears that there is no clear guideline for the selection of the dilation angle α for concrete.

In the K&C concrete damage model, a partially associated flow rule is used. This flow rule is characterised by an input parameter ω, which represents the ratio of an associated plastic flow to the Prandtl-Reuss plastic flow. The plastic flow is purely deviatoric for $\omega = 0$ and is associative for $\omega = 1$, and it is interpolated between the two for $0 < \omega < 1$ (Baylot and Bevins 2007). It enables a control over the amount of plastic volume change in the material.

To investigate the effects of the shear dilation on the structural behaviour of the FRP-concrete bonded joint, the experimental specimen I-6 reported in Yao (2004) was modelled using various ω values. The specimen had a concrete strength $f_c' = 23.8\,MPa$. The load-slip curves from the numerical simulation are compared with the experimental data in Figure 6. It is seen that ω taking a value around 0.3 tends to result in a reasonable fit to the test results for this specimen. As shown in Figure 7, the peak load increases almost linearly with the increase of ω for both concrete strength levels. Figures 8 and 9 show the different evolution processes of pressure and damage from using different ω values. A larger ω value (e.g. 0.5 in Figure 9) produces higher pressures and a deeper debonding zone as compared with the results from using a smaller ω value (e.g. 0.3 in Figure 8). This may be explained by the fact that a higher shear dilation tends to lead to stronger confinement, thus involving more concrete to resist debonding and consequently a higher loading capacity.

A few more FRP-concrete bonded joint experiments with different f_c' were modelled using the K&C model with various ω, including IV-12 and III-7 in Yao *et al.*(2005), C4 in Wu *et al.* (2010) and B-1 in Ueda *et al.* (1999). The ω values which produce the best fit peak loads for the corresponding specimens are listed in Table 2. From these results, an empirical formula for the "best-fit" ω is obtained as a function of f_c' as:

$$\omega = 4\times10^{-6} f_c'^3 - 0.0003 f_c'^2 + 0.009 f_c' + 0.2 \tag{15}$$

Figure 10 illustrates the above relationship. To examine the applicability of this empirical equation, a large number of FRP-concrete bonded joints tests reported in Wu *et al.* (2010), Yao (2004), Wu *et al.* (2001) and Ueda *et al.*(1999) were modelled, using ω values calculated using Eqn 15. All the selected experimental specimens failed by debonding in concrete. Table 3 summarises the key parameters and the experimental, FE (P_{FE}) and predicted (by Chen and Teng's (2001) model, P_{pred}) peak loads. The ratios of the peak loads predicted from the current FE model to the experimental counterparts are also plotted in Figure 11. It can be seen that the FE model using ω values from Eqn 15 resulted in good agreement.

5 LOADING RATE EFFECTS ON FRP-TO-CONCRETE BOND BEHAVIOUR

5.1 *Dynamic Increasing Factor (DIF) of Concrete Strength*

For concrete structures subjected to transient dynamic loadings, the strain rate can be very high (e.g. up to $1000s^{-1}$ for blast). At such high strain rates, the apparent or engineering strength of concrete can increase significantly. This is often described by the ratio of the dynamic to static strength, namely, the dynamic increase factor (DIF). For concrete, the DIF can be larger than 2 in compression and 6 in tension at high strain rates on or above the order of $100s^{-1}$ (Malvar and Crawford 1998). The function relating DIF to the strain rate is treated as a material property in the K&C concrete damage model. The CEB-FIP (1993) DIF curve for concrete in compression was adopted in this study:

$$\text{DIF}= f_c / f_{cs} = (\dot{\varepsilon} / \dot{\varepsilon}_s)^{1.026\alpha_s} \text{ for } \dot{\varepsilon} \le 30s^{-1} \tag{16}$$

$$\text{DIF}= f_c / f_{cs} = \gamma_s (\dot{\varepsilon} / \dot{\varepsilon}_s)^{1/3} \text{ for } \dot{\varepsilon} > 30s^{-1} \tag{17}$$

where $\dot{\varepsilon}$ is the strain rate (from 30×10^{-6} to $300s^{-1}$), $\dot{\varepsilon}_s$ is the reference static strain rate and is assumed to be $30\times10^{-6}s^{-1}$, f_c is the dynamic compressive strength at $\dot{\varepsilon}$, f_{cs} is the static compressive strength at $\dot{\varepsilon}_s$, and

$$\log \gamma_s = 6.456\alpha_s - 2 \tag{18}$$

$$\alpha_s = 1/(5 + 9 f_{cs} / f_{co}) \tag{19}$$

Here, $f_{co} = 10MPa$

For concrete in tension with strain rates between 10^{-6} and $160s^{-1}$, the Modified CEB-FIP curve proposed by Malvar and Crawford (1998) was used in this study:

$$\text{DIF}= f_t / f_{ts} = (\dot{\varepsilon} / \dot{\varepsilon}_s)^{\delta} \text{ for } \dot{\varepsilon} \le 1s^{-1} \tag{20}$$

$$\text{DIF}= f_t / f_{ts} = \beta (\dot{\varepsilon} / \dot{\varepsilon}_s)^{1/3} \text{ for } \dot{\varepsilon} > 1s^{-1} \tag{21}$$

where f_t is the dynamic tensile strength at $\dot{\varepsilon}$, f_{ts} is the static tensile strength at $\dot{\varepsilon}_s = 10^{-6}s^{-1}$, and

$$\log \beta = 6\delta - 2 \tag{22}$$

$$\delta = 1/(1 + 8 f_{cs} / f_{co}) \quad (23)$$

5.2 *Dynamic Effect in Single Shear Test*

The same specimen S-CFS-400-25 in Wu *et al.* (2001) modelled in the static analyses presented in Section 4 was used as the reference case in the dynamic analyses here. The same geometry and boundary conditions in Figure 1 were adopted. The static concrete properties (as from the experiment) were used together with the DIF described above to model the dynamic behaviour of concrete. The mesh remained the same as in the static analyses with 1*mm* uniform 8-noded brick elements. The dynamic load was applied via a velocity history as shown in Figure 12 such that debonding was made to occur at the constant velocity phase. Different loading rates were achieved by adjusting the constant velocity values.

Figure 13 shows the load-slip curves from different loading rates applied at the loading end of the FRP. It can be seen that both the peak load and the maximum slip increase with the loading rate. For example, when the loading rate was increased from 0.1 *mm/s* to 100*mm/s*, P_u increased from 18.3*kN* to 44.3*kN*, while the maximum slip increased from 0.25*mm* to 2.0*mm*. This result demonstrates clearly that as the tensile strength and the fracture energy of concrete increases under dynamic loading, the dynamic FRP-to-concrete bond behaviour also enhances significantly.

Figure 14 shows the damage contours of the specimen at the ultimate state from different loading rates. It can be clearly observed that the damage zone also expands as the loading rate increases. This indicates that, as the loading rate increases, more concrete is involved in resisting the pull-off load, and hence delays debonding and increases the loading capacity.

Based on the preliminary dynamic analyse discussed above, it may reasonably be concluded that the loading rate has a significant effect on the FRP-to-concrete bond behaviour. It shall also be noted that the study here assumed that the debonding failure occurs in concrete, so that other failure modes, such as cohesive failure in the adhesive and interfacial debonding failure at the FRP-adhesive interface and at the adhesive-concrete interface do not occur. Whilst these failure modes are rare under static condition, it is not necessarily the case under dynamic condition and they can well become critical if their DIF values are lower than those of the concrete. These questions should be looked into in the follow-up research.

6 **CONCLUSIONS**

Modelling of fracture in concrete is an important topic, and this is particularly so when a finite element analysis with a local material damage model is employed. Mesh-objectivity cannot be achieved without an appropriate consideration of the localization in the finite element model and its relationship to the fracture energy. For meso-scopic modelling where the element size is smaller than the standard concrete aggregate size, the localized width (or crack band) should be set as the element characteristic length, especially in tension-dominated problems where the localization generally takes place in a single element. The results reported in this paper confirms that, by obeying its localization rule, the uni-axial tension and compression stress strain curve in a single element is rendered mesh dependent, but the overall behaviour

becomes essentially mesh-independent because the tension and fracture energy are kept as a constant.

This paper has presented a study on the modelling of the FRP-to-concrete bond behaviour using the K&C concrete damage model in LSDYNA with the explicit integration scheme, starting from the static case. The proposed FE model uses the first order eight node hexahedron 3D solid elements with one integration point and sub-millimetre mesh. The model has been demonstrated to be capable of simulating the static FRP-to-concrete bond behaviour, given proper consideration of strain localization and dilation of concrete. The load-carrying capacity, load-displacement behaviour and local bond-slip behaviour were predicted with reasonable accuracy and mesh objectivity.

An important observation from this study is that the dilation of concrete has an important effect on the simulation results for the type of problems under investigation. A large dilation angle tends to increase the confinement of concrete, thus leading to higher loading capacity. An empirical relationship between the dilation parameter and the concrete strength for simulating FRP-to-concrete bond behaviour has been proposed.

A preliminary study on the effect of dynamic loading rate on the behaviour of FRP-to-concrete bonded joint has been presented. By considering the dynamic increase factor for concrete strength as a function of the strain rate, the effects of loading rate on the load-slip curve, effective bond length, ultimate load and the damaged concrete zone were explored. The developed numerical model and results will be useful for the numerical simulation and improved understanding of the structural behaviour of FRP-strengthened concrete structures under dynamic loadings such as impact, blast and earthquakes.

ACKNOWLEDGEMENTS

The authors are grateful for financial support from National Basic Research Program (i.e. 973 Program) (Project No. 2012CB026200) of China, National Science Foundation of China (NSFC) (No. 51308271), Yunnan Provincial Department of Science and Technology (General Project on Applied Basic Research, Grand No.2013FB018) and a scholarship provided to the first author by EPSRC (UK) and Royal Dutch Shell plc through a Dorothy Hodgkin Postgraduate Award.

REFERENCES

Baylot, J.T. and Bevins, T.L. (2007). "Effect of responding and failing structural components on the airblast pressures and loads on and inside of the structure", *Computers and Structures*, Vol. 85, No. 11-14, pp. 891–910.

Bazant, Z.P. and Oh, B.H. (1983). "Crack band theory for fracture of concrete", *Materials and Structures (RILEM, Paris)*, Vol.16, No.3, pp. 155–177.

Bazant, Z.P. and Ozbolt, J. (1990). "Nonlocal Microplane Model for Fracture, Damage, and Size Effect in Structures", *Journal of Engineering Mechanics*, Vol. 116, No. 11, pp. 2485-2505.

Bazant, Z. P. and Pijaudier-Cabot, G. (1988). "Nonlocal continuum damage, localization instability and convergence", *Journal of Applied Mechanics*, Vol. 55, No. 2, pp. 287-293.

Bhatti, A.Q., Kishi, N. and Tan, K. (2011). "Impact resistant behaviour of RC slab strengthened with FRP sheet", *Materials and Structures*, Vol. 44, No. 10, pp. 1855-1864.

Boyd, A.J., Liang, N., Green, P.S. and Lammert, K. (2008). "Sprayed FRP repair of simulated impact in prestressed concrete girders", *Construction and Building Materials*, Vol. 22, No.3, pp. 411-16.

Buchan, P.A. and Chen, J.F. (2007). "Blast resistance of FRP composites and polymer strengthened concrete and masonry structures – a state-of-the-art review", *Composites, Part B: Engineering*, Vol. 38, No.5-6, pp. 509–522.

CEB-FIP (1993). *Model Code 1990 for concrete structures*. Comité euro-international du Béton(CEB), Laussane. Thomas Telford Services, Ltd. London, UK.

Chandra, S., Nilsen, B. and Lu, M. (2010). "Predicting excavation methods and rock support: a case study from the Himalayan region of India", *Bulletin of Engineering Geology and the Environment*, Vol. 69, No. 2, pp. 257–266.

Chen, G.M., Chen, J.F. and Teng, J.G. (2012). "On the finite element modelling of RC beams shear-strengthened with FRP", *Construction and Building Materials*, Vol.32, pp.13–26.

Chen, G.M., Teng, J.G. and Chen, J.F. (2011). "Finite element modelling of intermediate crack debonding in FRP-plated RC beams", *Journal of Composites for Construction, ASCE*, Vol. 15, No. 3, pp. 339-353.

Chen, G.M., Teng, J.G. and Chen, J.F. (2009). "Finite element simulation of IC debonding in FRP-plated RC beams: a dynamic approach", *The 9th International Symposium on Fibre Reinforced Polymer for Concrete Structures (FRPRCS9)*, 13-15 July, Sydney, Australia, pp. 13-15.

Chen, J.F., Yang, Z.J. and Holt, G.D. (2001). "FRP or steel plate-to-concrete bonded joints: effect of test methods on experimental bond strength", *Steel and Composite Structures*, Vol. 1, No. 2, pp. 231-244.

Chen, J.F. and Tao, Y. (2010). "Finite element modelling of FRP-to-concrete bond behaviour using a plastic degradation theory based concrete damage plasticity model", *Proceedings of the 5th International Conference on FRP Composites in Civil Engineering*, 27–29 September, Beijing, China, pp. 45-50.

Chen, J.F. and Teng, J.G. (2001). "Anchorage strength models for FRP and steel plates bonded to concrete", *Journal of Structural Engineering, ASCE*, Vol.127, No.7, pp. 784–791.

Crawford, J.E., Malvar, J., Wesevich, J.W. and Raynolds, A. D. (1997). "Retrofit of reinforced concrete structures to resist blast effects", *ACI Structural Journal*, Vol. 94, No. 4, pp. 371–377.

Crawford, J.E., Malvar, L.J., Morrill, K.B. and Ferritto, J.M. (2001). "Composite Retrofits to Increase the Blast Resistance of Reinforced Concrete Buildings", *Proceedings of the 10th International Symposium on Interaction of the Effects of Munitions with Structures*, May, San Diego, CA, pp. 1-13.

De Lorenzis, L. and La Tegola, A. (2005). "Bond of FRP laminates to concrete under impulse loading: a simple model", *Proc. International Symposium on Bond Behaviour of FRP in Structures (BBFS 2005)*, Hong Kong, China, pp. 503-508.

Heffernan, P.J., Wight, R.G. and Erki, M.A. (2011). "Research on the use of FRP for critical load-bearing infrastructure in conflict zones", *Journal of Composites for Construction*, Vol. 15, No. 2, pp. 136-145.

Kim, S.W. and Vecchio, F.J. (2008). "Modeling of shear-critical reinforced concrete structures repaired with fiber-reinforced polymer composites", *Journal of Structural Engineering*, Vol. 134, No. 8, pp. 1288-1299.

Li, X.Q., Chen, J.F. and Lu, Y. (2010). "Meso-scale modelling of FRP-to-concrete bond behaviour using LSDYNA", *Proceedings of the 5th International Conference on FRP Composites in Civil Engineering*, 27–29 September, Beijing, China, pp. 494-498.

Li, X. Q. (2012). *FRP-to-concrete bond behaviour under high strain rates*, PhD thesis, The University of Edinburgh, Edinburgh, UK.

LSTC (2007). *Keyword User's Manual Version 971*, Livermore Software Technology Corporation (LSTC), Livermore, CA.

Lu, X.Z., Teng, J.G., Ye, L.P. and Jiang, J.J. (2005). "Bond–slip models for FRP sheets/plates bonded to concrete", *Engineering Structures*, Vol. 27, No. 6, pp. 920–937.

Lu, X.Z., Ye, L.P., Teng, J.G. and Jiang, J.J. (2004). "Mesco-scale finite element model for FRP sheets/plates bonded to concrete", *Engineering structures*, Vol. 27, No. 4, pp. 564-575.

Lubliner, J. (1989). "A plastic-damage model for concrete", *International Journal of Solids and Structures*, Vol. 25, No. 3, pp. 299–326.

Malvar, L.J. and Crawford, J.E. (1998). *Dynamic increasing factors for concrete*, Naval facilities engineering service center, Port Hueneme, CA.

Malvar, L.J., Crawford, J.E. and Morrill, K.B. (2000). *K&C Concrete material model release3—automated generation of material model input*, Technical Report TR-99-24.3, Karagozian and Case Structural Engineers, Glendale, CA.

Malvar, L.J., Crawford, J.E., Wesevich, J.W. and Simons, D. (1997). "A plasticity concrete material model for DYNA3D", *International Journal of Impact Engineering*, Vol. 19, No. 9-10, pp. 847-873.

Malvar, L.J. and Simons, D. (1996). "Concrete material modeling in explicit computations", *Proceedings of the Workshop on Recent Advances in Computational Structural Dynamics and High Performance Computing*, USAE Waterways Experiment Station, April 24-26, Vicksburg, MS, pp. 165-194.

Markovich, N., Kochavi, E. and Ben-Dor, G. (2011). "An improved calibration of the concrete damage model", *Finite Elements in Analysis and Design*, Vol. 47, No. 11, pp. 1280–1290.

Niroomandi, A., Maheri, A., Maheri, M., R. and Mahini, S.S. (2010). "Seismic performance of ordinary RC frames retrofitted at joints by FRP sheets", *Engineering Structures*, Vol. 32, No 8, pp. 2326-2336.

Pantelides, C.P. and Gergely, J. (2007). "Seismic retrofit of reinforced concrete beam-column T-joints in bridge piers with FRP composite jackets", American Concrete Institute, *ACI Special Publication*, Vol. 258, pp. 1-18.

Schwer, L.E. and Malvar, L.J. (2005). "Simplified concrete modeling with *mat_concrete_damage_rel3", *JRI LS-Dyna User Week*, Nagoya, Japan, pp. 49-60.

Su, X.T., Yang, Z.J. and Liu, G.H. (2010). "Monte Carlo simulation of complex cohesive fracture in random heterogeneous quasi-brittle materials: a 3D study", *International Journal of Solids and Structures*, Vol. 47, No. 17, pp. 2336-2345.

Tarapada, R. and Debabrata, C. (2006). "Delamination in hybrid FRP laminates under low velocity impact", *Journal of Reinforced Plastics and Composites*, Vol. 25, No. 18, pp. 1939-56.

Teng, J.G., Chen, J.F., Smith, S.T. and Lam, L. (2002). *FRP-Strengthened RC Structures*, John Wiley and Sons, Chichester, UK.

Teng, J.G., Zou, X.K., De Lorenzis, L. and Xia, S.H. (2007). "Optimal performance-based design of FRP jackets for seismic retrofit of reinforced concrete frames", *Composites Part B: Engineering*, Vol. 38, No. 5-6, pp. 584-97.

Tu, Z.G. and Lu, Y. (2009). "Evaluation of typical concrete material models used in hydrocodes for high dynamic response simulations", *International Journal of Impact Engineering*, Vol. 36, No. 1, pp. 132-146.

Ueda, T., Sato, Y. and Asano, Y. (1999). "Experimental study on bond strength of continuous carbon fiber sheet", *ACI Special Publication*, Vol. 188, pp. 407-416.

Wu, C., Oehlers, D.J. and Day, I. (2009). "Layered blast capacity analysis of FRP retrofitted RC member", *Advances in Structural Engineering*, Vol. 12, No. 3, pp. 435-449.

Wu, Y.F., Zhou, Z.Q., Yang, Q.D. and Chen, W.Q. (2010). "On shear bond strength of FRP-concrete structures", *Engineering Structures*, Vol. 32, No. 3, pp. 897-905.

Wu, Z.S., Yuan, H., Yoshizawa, H. and Kanakubo, T. (2001). "Experimental/analytical study on interfacial fracture energy and fracture propagation along FRP-concrete interface", *ACI Special Publication*, Vol.201, pp. 133–152.

Yang, Z.J., Chen, J.F. and Proverbs, D. (2003). "Finite element modelling of concrete cover separation failure in FRP plated RC beams", *Construction and Building Materials*, Vol. 17, No. 1, pp. 3-13.

Yang, Z.J., Su, X.T., Chen, J.F. and Liu, G.H. (2009). "Monte Carlo simulation of complex cohesive fracture in random heterogeneous quasi-brittle materials", *International Journal of Solids and Structures*, Vol. 46, No. 17, pp. 3222-3234.

Yao, J. (2004). *Debonding failures in reinforced concrete structures strengthened with externally bonded FRP sheets/plates*, PhD Thesis, Department of Civil and Structural Engineering, Hong Kong Polytechnic University, Hong Kong.

Yao, J., Teng, J.G. and Chen, J.F. (2005). "Experimental study on FRP-to-concrete bonded joints", *Composites Part B: Engineering*, Vol. 36, No. 2, pp. 99-113.

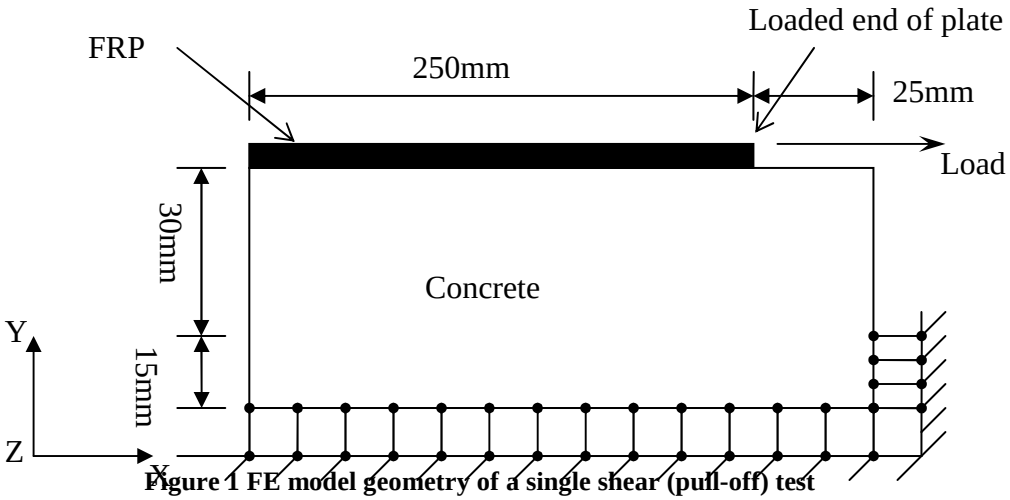

Figure 1 FE model geometry of a single shear (pull-off) test

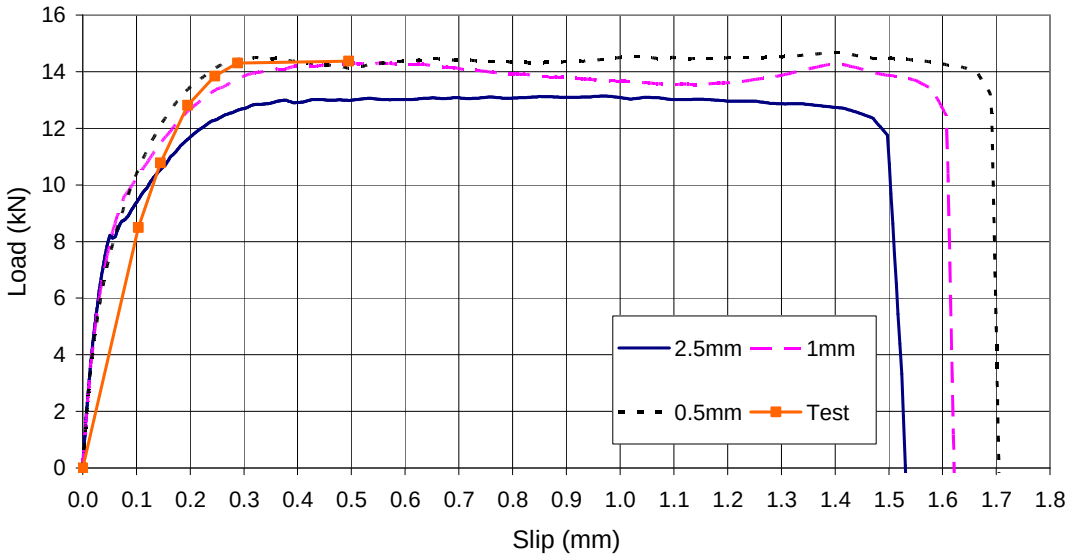

Figure 2 Load-slip curves: mesh convergence

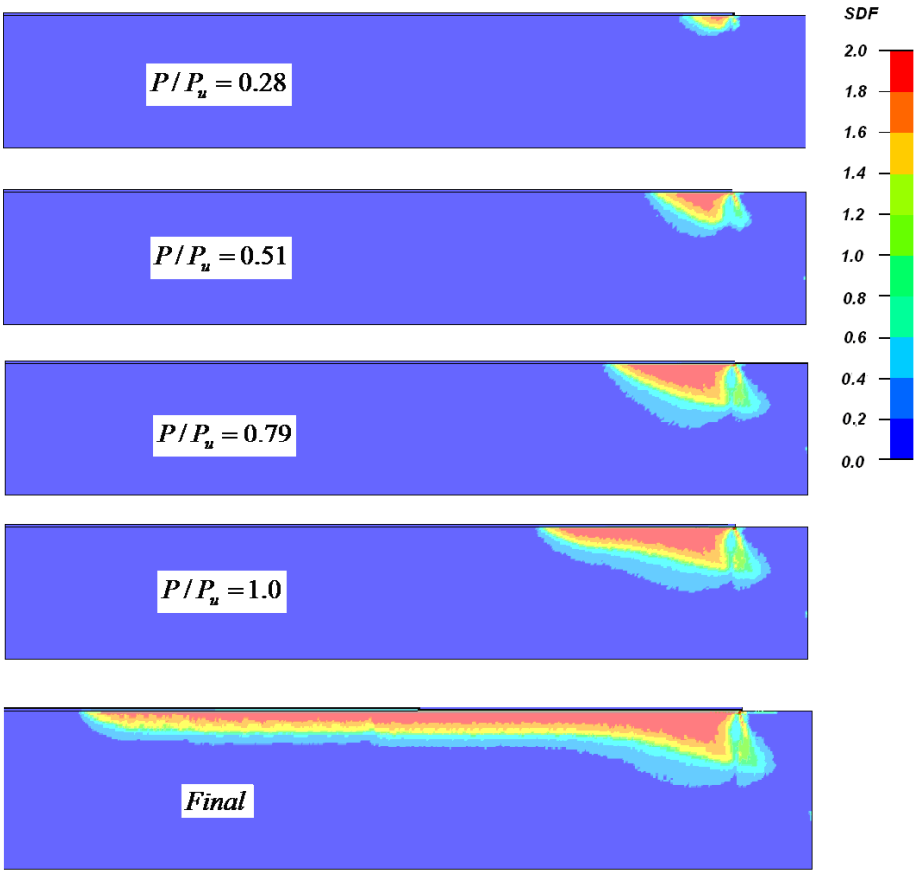

Figure 3 Damage contours showing development of damage as load increases

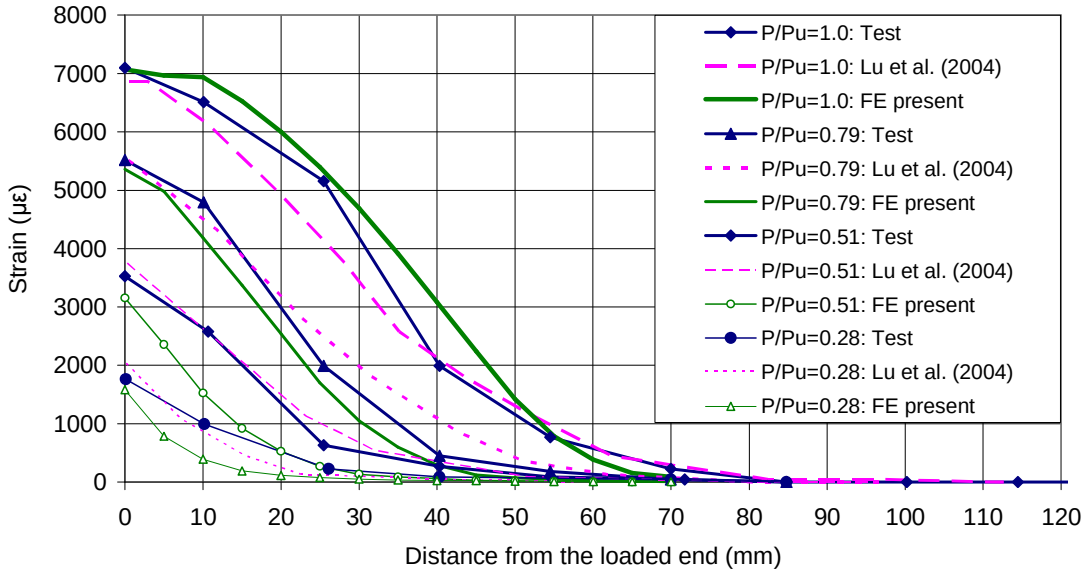

Figure 4 FRP strain distributions at different loading stages

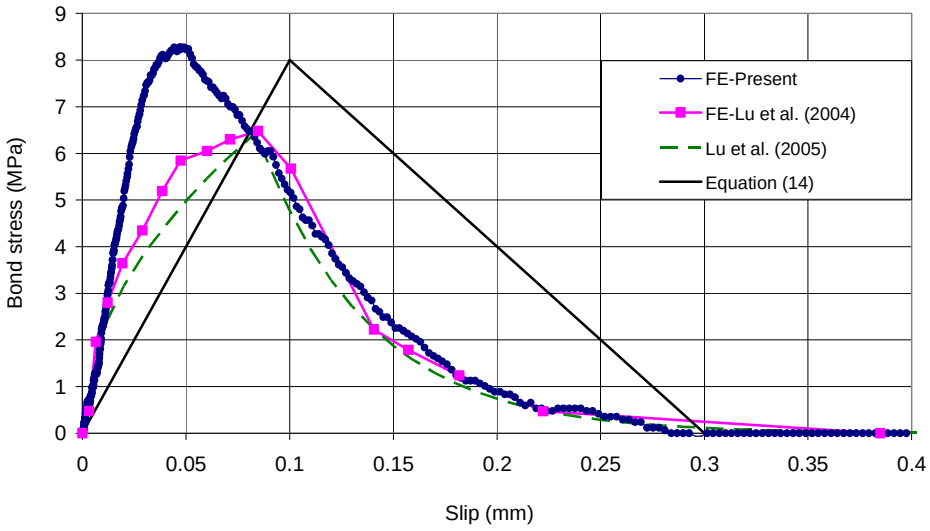

Figure 5 Local bond stress - slip curves

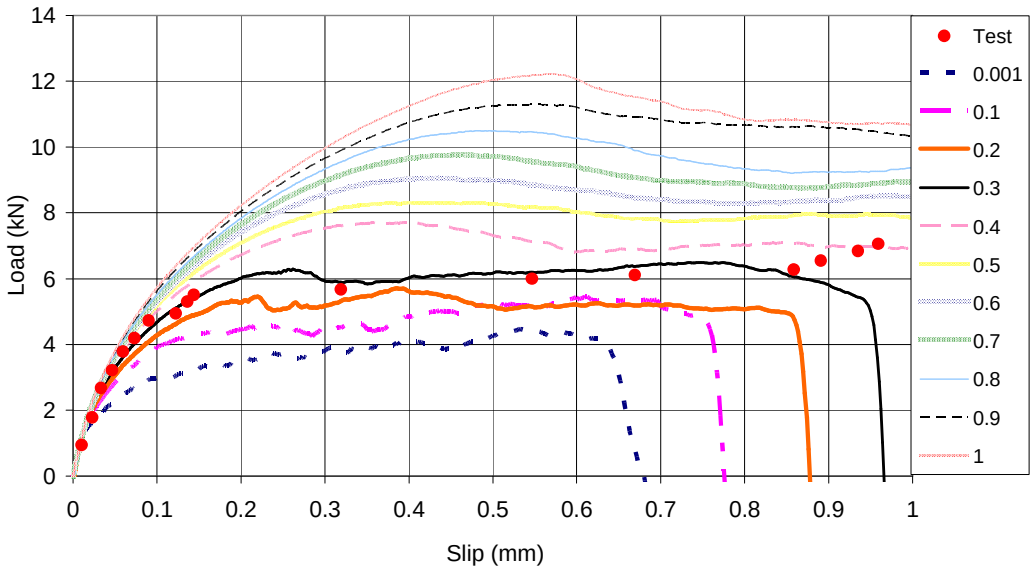

Figure 6 Effect of ω on the FE predicted load slip curves: concrete strength $f_c' = 23.8MPa$, test result from Yao (2004)

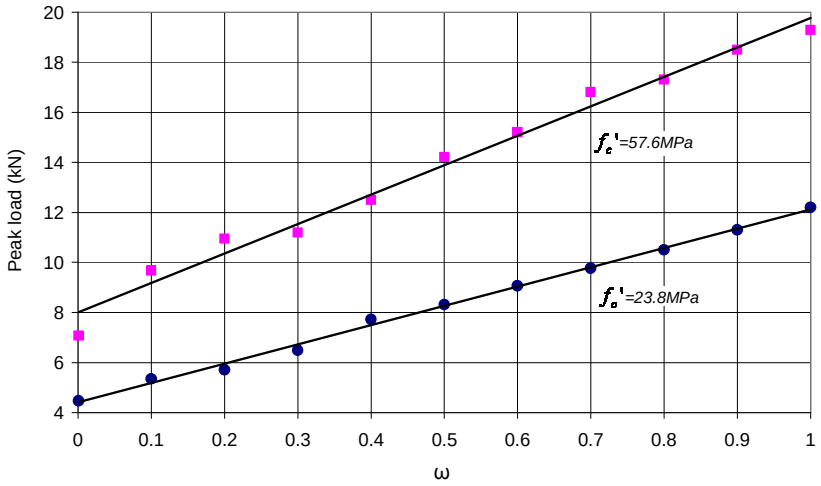

Figure 7 Relationship between ω and the predicted peak Load

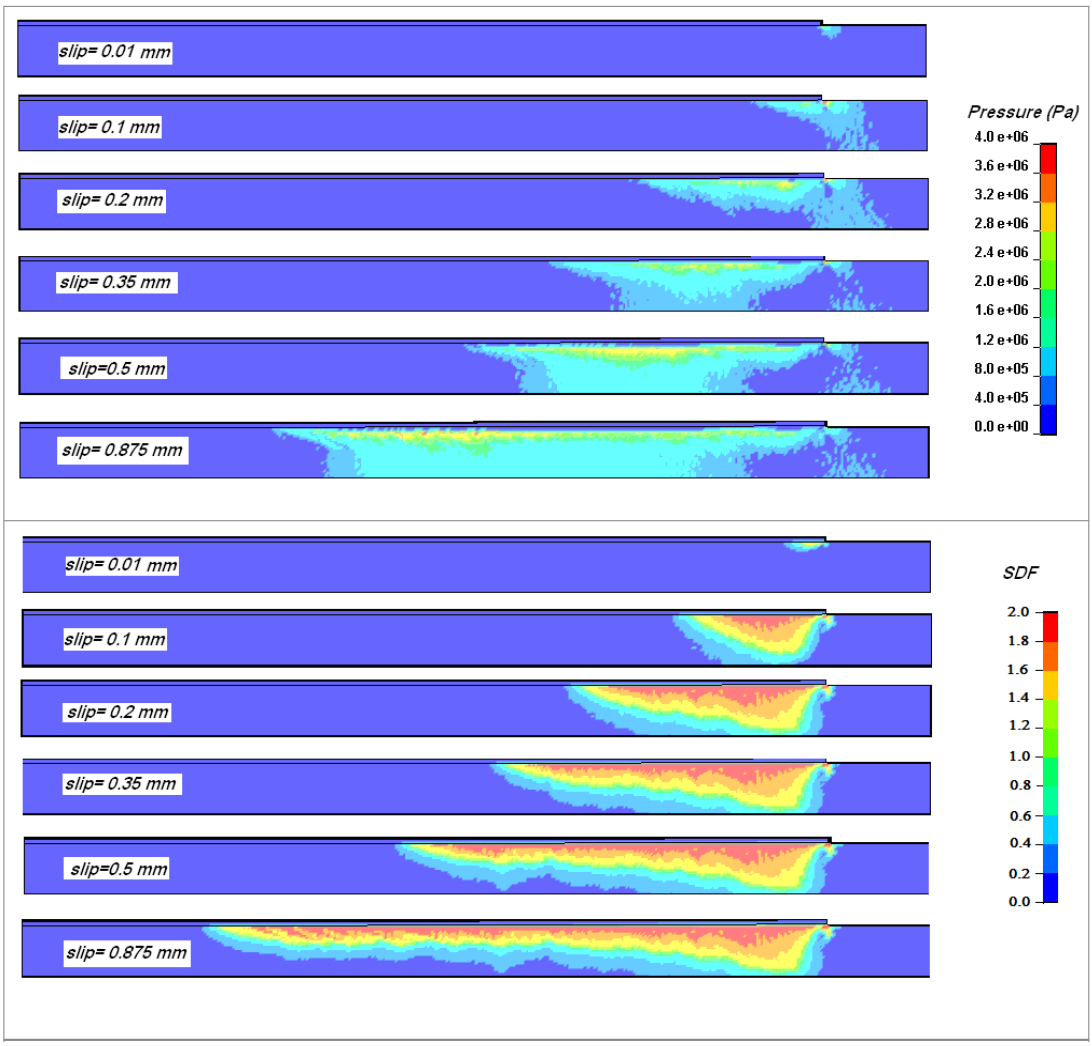

Figure 8 Development of pressure and damage (SDF) for ω=0.3

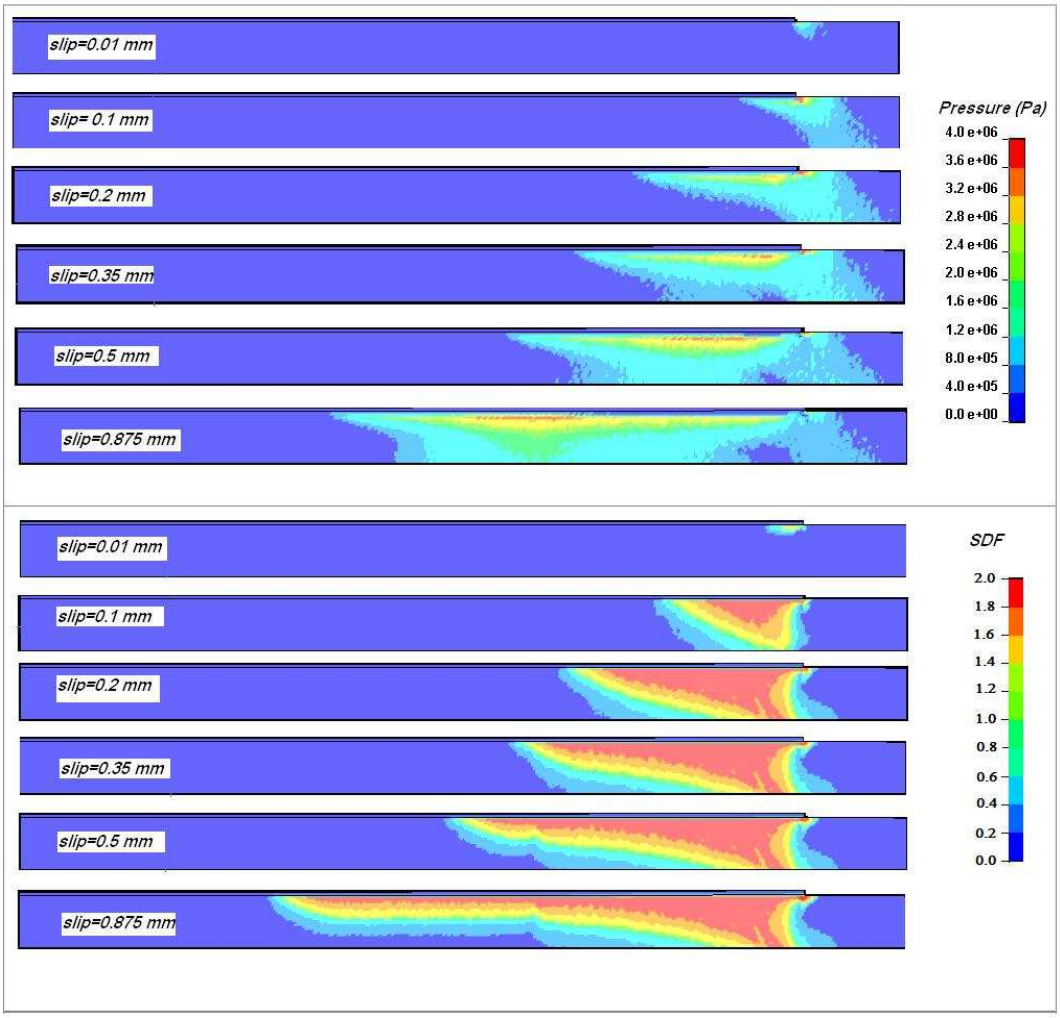

Figure 9 Development of pressure and damage (SDF) for ω=0.5

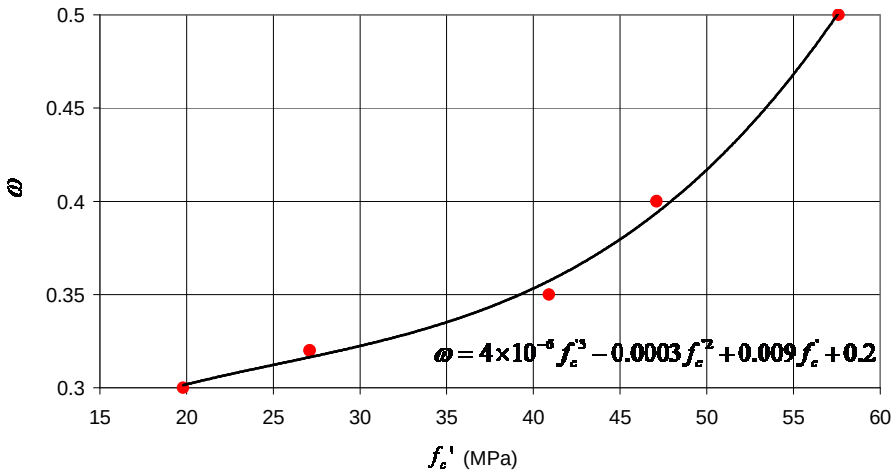

Figure 10 Relationship between "best-fit" ω and f_c'

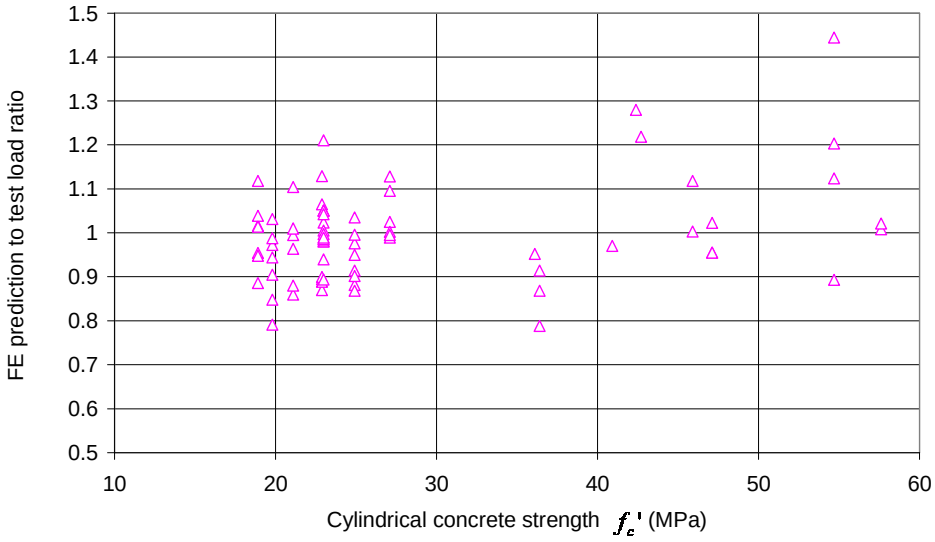

Figure 11 FE predicted to experimental ultimate load ratio for a variety of experiments

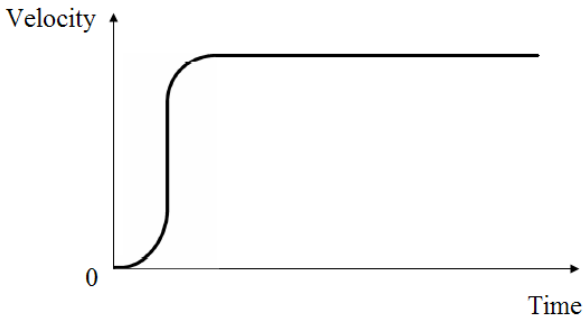

Figure 12 A velocity-controlled loading scheme with a smooth start

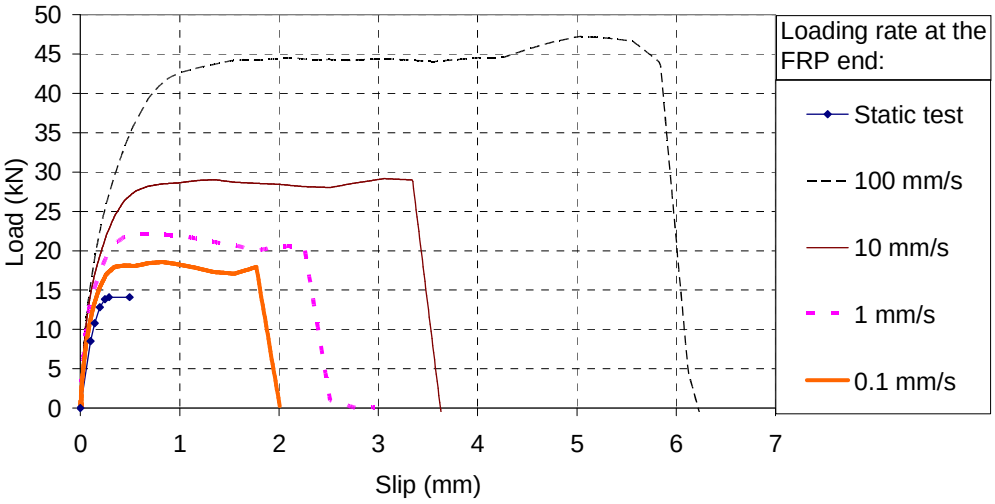

Figure 13 Strain rate effects on pull-off behaviour

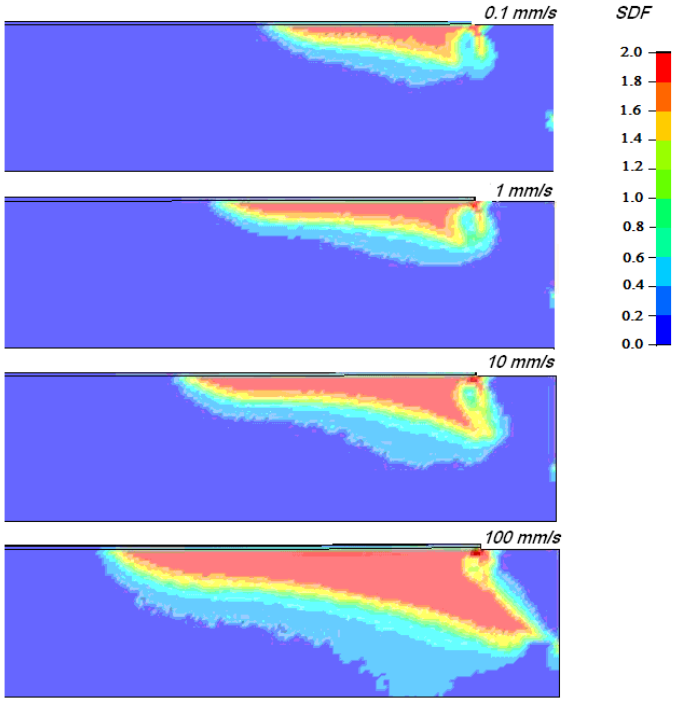

Figure 14 Contour of scaled damage factor for the reference specimen when the maximum load is attained under different loading rates (note that only part of the model is shown)

Table 1 Parameters for the reference case

a_{0y}	a_{1y}	a_{2y}		λ_1	λ_2	λ_3	λ_4	λ_5	λ_6	λ_7
1.3×10^{7}	6.2×10^{-1}	4.5×10^{-9}		0.0	8×10^{-6}	2.4×10^{-5}	4.0×10^{-5}	5.6×10^{-5}	7.2×10^{-5}	8.8×10^{-5}
a_0	a_1	a_2		η_1	η_2	η_3	η_4	η_5	η_6	η_7
1.7×10^{7}	4.5×10^{-1}	1.4×10^{-9}		0.0	0.85	0.97	0.99	1.0	0.99	0.97
a_{1f}	a_{2f}			λ_8	λ_9	λ_{10}	λ_{11}	λ_{12}	λ_{13}	
4.4×10^{-1}	2.0×10^{-9}			3.2×10^{-4}	5.7×10^{-4}	5.4×10^{-4}	1.0	10	1.0×10^{10}	
f_c'	f_t	ω		η_8	η_9	η_{10}	η_{11}	η_{12}	η_{13}	
$57.6MPa$	$4.02MPa$	0.5		0.5	0.1	0.01	0.001	0.0001	0.0	
b_1	b_2	r_f								
1.6	0.45	0								

Table 2 Best-fit peak load and dilation parameter ω (data for deriving Eqn 15)

Test specimen	$f_c^{'}(MPa)$	ω	P_{Test}	P_{FE}
IV-12	19.8	0.3	5.67	5.60
III-7	27.1	0.32	4.78	4.73
B-1	40.9	0.35	20.60	19.99
C4	47.1	0.4	10.64	10.16
WU-1	57.6	0.5	14.1	14.21

Table 3 Parameters of test specimens and FE prediction with concrete dilation based on Eqn 15

Specimen	f_c' (MPa)	b_c (mm)	b_p (mm)	L (mm)	E_p (GPa)	t_p (mm)	ω	P_{pred} (kN)	P_{test} (kN)	P_{FE} (kN)	P_{FE}/P_{test}	P_{pred}/P_{test}
IV-1	18.9	150	25	95	256	0.165	0.30	5.72	5.86	5.59	0.95	1.02
IV-2	18.9	150	25	95	256	0.165	0.30	5.72	5.90	5.59	0.95	1.02
IV-5	18.9	150	25	95	256	0.165	0.30	5.72	5.00	5.59	1.12	1.02
IV-7	18.9	150	25	95	256	0.165	0.30	5.72	5.50	5.59	1.02	1.02
IV-9	18.9	150	25	95	256	0.165	0.30	5.72	5.38	5.59	1.04	1.02
IV-11	18.9	150	25	95	256	0.165	0.30	5.72	5.51	5.59	1.01	1.02
IV-3	19.8	150	25	95	256	0.165	0.30	5.8	5.43	5.60	1.03	1.04
IV-4	19.8	150	25	95	256	0.165	0.30	5.8	5.76	5.60	0.97	1.04
IV-6	19.8	150	25	95	256	0.165	0.30	5.8	7.08	5.60	0.79	1.04
IV-8	19.8	150	25	95	256	0.165	0.30	5.8	5.93	5.60	0.94	1.04
IV-10	19.8	150	25	95	256	0.165	0.30	5.8	6.60	5.60	0.85	1.04
IV-12	19.8	150	25	95	256	0.165	0.30	5.8	5.67	5.60	0.99	1.04
IV-14	19.8	150	25	95	256	0.165	0.30	5.8	6.19	5.60	0.90	1.04
V-1	21.1	150	15	95	256	0.165	0.30	3.71	3.81	3.79	0.99	0.98
V-2	21.1	150	15	95	256	0.165	0.30	3.71	4.41	3.79	0.86	0.98
V-3	21.1	150	25	95	256	0.165	0.30	5.89	6.26	6.03	0.96	0.98
V-4	21.1	150	50	95	256	0.165	0.30	10.51	12.22	10.75	0.88	0.98
V-5	21.1	150	75	95	256	0.165	0.30	14.1	14.29	14.43	1.01	0.98
V-6	21.1	150	100	95	256	0.165	0.30	16.82	15.58	17.20	1.10	0.98
II-1	22.9	150	25	95	256	0.165	0.30	6.02	5.20	5.87	1.13	1.03
II-2	22.9	150	25	95	256	0.165	0.30	6.02	6.75	5.87	0.87	1.03
II-3	22.9	150	25	95	256	0.165	0.30	6.02	5.51	5.87	1.07	1.03
II-4	22.9	150	25	190	256	0.165	0.30	6.02	7.02	6.28	0.89	0.96
II-5	22.9	150	25	190	256	0.165	0.30	6.02	7.07	6.28	0.89	0.96
II-6	22.9	150	25	190	256	0.165	0.30	6.02	6.98	6.28	0.90	0.96
I-1	23	150	25	75	256	0.165	0.30	5.72	4.75	5.75	1.21	0.99
I-2	23	150	25	85	256	0.165	0.30	5.96	5.69	5.98	1.05	1.00
I-3	23	150	25	95	256	0.165	0.30	6.02	5.76	6.05	1.05	1.00
I-4	23	150	25	95	256	0.165	0.30	6.02	5.76	6.05	1.05	1.00
I-5	23	150	25	95	256	0.165	0.30	6.02	6.17	6.05	0.98	1.00
I-6	23	150	25	115	256	0.165	0.30	6.02	5.96	6.10	1.02	0.99
I-7	23	150	25	145	256	0.165	0.30	6.02	5.95	6.20	1.04	0.97
I-8	23	150	25	190	256	0.165	0.30	6.02	6.68	6.28	0.94	0.96
I-9	23	150	25	190	256	0.165	0.30	6.02	6.35	6.28	0.99	0.96
I-10	23	150	25	95	256	0.165	0.30	6.02	6.17	6.05	0.98	1.00
I-11	23	150	25	75	256	0.165	0.30	5.72	5.72	5.75	1.01	0.99
I-12	23	150	25	85	256	0.165	0.30	5.96	6.00	5.98	1.00	1.00
I-13	23	150	25	95	256	0.165	0.30	6.02	6.14	6.05	0.99	1.00
I-14	23	150	25	115	256	0.165	0.30	6.02	6.19	6.10	0.99	0.99
I-15	23	150	25	145	256	0.165	0.30	6.02	6.27	6.20	0.99	0.97
I-16	23	150	25	190	256	0.165	0.30	6.02	7.03	6.28	0.89	0.96
VII-1	24.9	150	25	95	256	0.165	0.31	6.14	6.80	6.46	0.95	0.95

Specimen	f_c' (MPa)	b_c (mm)	b_p (mm)	L (mm)	E_p (GPa)	t_p (mm)	ω	P_{pred} (kN)	P_{test} (kN)	P_{FE} (kN)	P_{FE}/P_{test}	P_{pred}/P_{test}
VII-2	24.9	150	25	95	256	0.165	0.31	6.14	6.62	6.46	0.98	0.93
VII-3	24.9	150	25	145	256	0.165	0.31	6.14	7.33	6.46	0.88	0.84
VII-4	24.9	150	25	145	256	0.165	0.31	6.14	6.49	6.46	1.00	0.95
VII-5	24.9	150	25	190	256	0.165	0.31	6.14	7.07	6.46	0.91	0.87
VII-6	24.9	150	25	190	256	0.165	0.31	6.14	7.44	6.46	0.87	0.83
VII-7	24.9	150	25	240	256	0.165	0.31	6.14	7.16	6.46	0.90	0.86
VII-8	24.9	150	25	240	256	0.165	0.31	6.14	6.24	6.46	1.04	0.98
III-1	27.1	150	25	100	256	0.165	0.32	6.27	5.94	6.70	1.13	1.06
III-2	27.1	150	50	100	256	0.165	0.32	11.19	11.66	11.95	1.02	0.96
III-3	27.1	150	75	100	256	0.165	0.32	15.02	14.63	16.03	1.10	1.03
III-4	27.1	150	100	100	256	0.165	0.32	17.91	19.07	19.12	1.00	0.94
III-7	27.1	100	25.3	100	22.5	1.27	0.32	4.92	4.78	4.73	0.99	1.03
III-8	27.1	100	50.6	100	22.5	1.27	0.32	8.3	8.02	7.98	1.00	1.03
C1	36.1	228.6	25.4	76.2	108	1.016	0.33	8.90	8.46	8.05	0.95	1.05
C14	36.4	228.6	25.4	101.6	108	1.016	0.33	10.67	12.80	10.09	0.79	0.83
C15	36.4	152.4	25.4	152.4	108	1.016	0.33	10.86	11.90	10.33	0.87	0.91
C16	36.4	152.4	25.4	203.2	108	1.016	0.33	11.09	11.57	10.58	0.91	0.96
B-1	40.9	500	100	200	230	0.11	0.35	21.04	20.60	19.99	0.97	1.02
M4	42.4	100	50	75	380	0.165	0.36	12.72	10.00	12.80	1.28	1.27
M6	42.7	100	50	65	230	0.22	0.36	11.26	9.55	11.64	1.22	1.18
B-2	45.9	500	100	200	230	0.33	0.38	37.50	38.00	38.11	1.00	0.99
B-3	45.9	500	100	200	230	0.33	0.38	37.50	34.1	38.11	1.12	1.10
C2	47.1	228.6	25.4	76.2	108	1.016	0.39	9.96	9.93	10.16	1.02	1.00
C3	47.1	228.6	25.4	76.2	108	1.016	0.39	9.96	10.64	10.16	0.95	0.94
C4	47.1	228.6	25.4	76.2	108	1.016	0.39	9.96	10.64	10.16	0.95	0.94
C100_50A	54.7	200	50	100	170	1.25	0.46	25.32	17.30	24.98	1.44	1.46
C200_50A	54.7	200	50	200	170	1.25	0.46	31.67	27.50	30.90	1.12	1.15
C300_50A	54.7	200	50	300	170	1.25	0.46	31.67	35.10	31.33	0.89	0.90
C400_50A	54.7	200	50	400	170	1.25	0.46	31.67	26.90	32.37	1.20	1.18
WU-1	57.6	100	40	250	230	0.22	0.5	11.32	14.10	14.21	1.01	0.80
WU-2	57.6	100	40	250	390	0.501	0.5	22.24	23.50	24	1.02	0.95
Average											0.997	0.999
CoV											10.9%	9.34%